48th AIAA Aerospace Sciences Meeting Including the New Horizons Forum and Aerospace Exposition
4 - 7 January 2010, Orlando, Florida

AIAA 2010-53

Delayed Detached Eddy Simulation of 3-D Wing Flutter with Fully Coupled Fluid-Structural Interaction

Xiangying Chen,[*] Baoyuan Wang,[†] and Ge-Cheng Zha[‡]
Dept. of Mechanical and Aerospace Engineering
University of Miami
Coral Gables, Florida 33124

Abstract

This paper presents a strategy using a high fidelity delayed-detached-eddy simulation (DDES) to simulate 3-D fluid-structural interaction for predicting AGARD Wing 445.6 flutter boundary in a transonic flow. A dual-time step implicit unfactored Gauss-Seidel iteration with Roe scheme are employed for the flow solver. The special numerical techniques used herein include: a 5th order WENO scheme for the inviscid fluxes, and a fully conservative 4th order central differencing scheme for the viscous terms. A modal approach is used for the structural response. The flow and structural solvers are fully coupled vis successive iterations within each physical time step. The method is implemented as a massive parallel solver in a MPI environment. The computed flutter boundary of AGARD Wing 445.6 in a transonic flow agrees well with the experiment and the prediction made by other method.

Keywords: Delayed-detached-eddy simulation; Transonic wing flutter; Fluid-structural interaction

1 Introduction

A flutter boundary of an airfoil or a wing is formed by a set of critical values of the flutter speed index (FSI), and divides the FSI-Mach number plane into a damped region and a diverging one. Flutter occurs as a result of the fluid-structural interaction and is usually involved with complicated fluid dynamic phenomena such as the shock wave/boundary layer interaction, and flow separation. When the value of FSI is greater than its critical upper limit for a certain Mach number, the

---

[*] Research Associate Professor
[†] PhD. Student
[‡] Associate Professor

Copyright © 2010 by the authors of this paper. Published by the American Institute of Aeronautics and Astronautics, Inc., with permission.

diverging flutter is initiated by any perturbation in the flow field. Due to the torsion flutter, the angle of attack (AOA) increases with time. In the case of airfoil/wing oscillating with small or moderate amplitude of AOA, the flow can still be attached. If the amplitude of AOA increases further during the oscillatory cycle, the flow separation, reattachment, and vortex shedding can be observed. Therefore, to accurately predict wing flutter, turbulence modelling is still the bottleneck to handling the complex flows with unsteady massive separation and reattachment.

Bendiksen et al.[1] pioneered the research by using an explicit Euler equation code coupled with a structural integrator based on the convolution integral to obtain the flutter boundary for a NACA 64A010 airfoil. In the study, the viscous effect on flutter boundary has been neglected. Later, Jameson [2] presented a multigrid time dependent Euler equation calculation for a pitching NACA 64A010 airfoil and pointed out the importance of viscosity effects in aeroelastic analysis. Alonso et al.[3] followed the same approach and used a multigrid unsteady Navier-Stokes code for aeroelastic calculations in which only the laminar viscosity is included. The early attempt to evaluate turbulence models in aeroelastic applications was made by Srinivasan et al.[4]. Five widely-used turbulence models for Reynolds averaged Navier-Stocks (RANS) equations, namely the Baldwin-Lomax model [5], the Renormalization Group model [6], the half-equation Johnson-King model [7, 8], and the one-equation models of Baldwin-Barth [9] and Spalart-Allmaras [10] are tested and evaluated for accuracy and robustness by using them to simulate the unsteady flows passing an oscillating NACA 0015 airfoil. Their conclusion is that the one-equation models provide significant improvement over the algebraic and half-equation models. Prananta et al.[11] reported the results of aeroelastic simulations by using the Euler and the Navier-Stokes solvers. Their calculations show that the viscous effect plays an extremely important role in determining the transonic dip and flutter boundary for a NACA64A010 airfoil. The work of Bohbot et al.[12] provides a comparison between the Baldwin-Lomax solution and Spalart-Allmaras solution of the viscous flutter boundary prediction for the same airfoil. A significant difference can be observed between two predicted flutter boundaries by the two turbulence models. Similar comparison between Euler and Navier-Stokes flutter results has been done by Lee-Rausch et al.[13] for AGARD Wing 445.6. Their calculation shows a significant viscous effect on the supersonic flutter boundary, and the Euler flutter result is quiet different from the Navier-Stokes one on the supersonic side. Similar Euler flutter results have been obtained by Liu et al.[14] for the same wing and flow conditions. The Euler solver performs poorly on the supersonic side of the flutter boundary. Another example of 3-D aeroelastic computations for transonic flows has been given by Doi et al.[15]. They found that the $k - \omega$ model [16] was the most suitable choice for prediction of flutter boundaries of turbomachinery components. Chen et al.[17, 18] have developed a fully coupled method between fluid and structure for 2-D flow-induced vibrations. Later, the method is extended to 3-D flutter prediction of flutter boundaries of AGARD Wing 445.6 using the Baldwin-Lomax model [19, 20].

As discussed above, the viscosity effects are important in aeroelastic analysis. It has been found that RANS models are inadequate to predict complex flow field with massive unsteady separated zones [4, 11, 12] for airfoil aeroelastic simulations. For wing aeroelastic simulations, the flow fields become much more complicated since a flexible wing has many more degrees of freedom than a rigid body airfoil that usually has two degrees of freedom. Therefore, an effort to explore an accurate, reliable and efficient turbulence closure in flexible wing aeroelastic simulations is crucial.

The objective of this investigation is to apply a recent turbulence simulation method, the delayed-detached-eddy simulation (DDES) suggested by Spalart et al.[21] for 3-D aeroelastic analysis. This is a first attempt to employ the DDES for prediction of flutter boundary of a flexible wing. In DES, a RANS model is used in the near-wall regions to reduce the grid density, and resolve the boundary layer flows in the manner of a RANS model, and the LES is used outside the near wall regions. Large eddy simulation (LES) has been proved to be a powerful method, and its first engineering application was reported by Deardorff [22] four decades ago. LES simulates the large scale structure of the flow field. The unresolved small scales need to be treated by a model since the small eddy structures are nearly isotropic and homogeneous in character, and hence much more reliable to be modeled. The drawback of LES is the requirement to use very fine grid in the near-wall regions. To bypass the problem, Spalart et al.[23] developed the DES as a hybrid between the LES and the Reynolds-averaged Navier-Stokes (RANS). DES is designed to take the advantages of both motheds, and to tackle the massively separated flows. Wang and zha[24] successfully applied the DES to predict the LCO of NLR7301 airfoil. An excellent quantitative agreement between the computation and experiement is achieved for both LCO frequency and amplitude. Delayed-detached-eddy simulation (DDES)[21] is a modified version of the original DES to overcome so-called modeled-stress depletion problem and make the DES limiter independendent of grid spacing.

In the present study, the high accuracy numerical techniques used include: a 5th order WENO scheme[25, 26] for the inviscid fluxes, and a fully conservative 4th order central differencing scheme[27] for the viscous terms. The high fidelity delayed-detached-eddy simulation (DDES) is used to predict the flutter boundary of AGARD Wing 445.6 in a transonic flow.

2 CFD Aerodynamic Model

2.1 Flow Governing Equations

After applying a spatially Favre-filtering process, the compressible Navier-Stokes equations can be transformed to the generalized coordinates and expressed as:

$$\frac{\partial \mathbf{Q}'}{\partial t} + \frac{\partial \mathbf{E}'}{\partial \xi} + \frac{\partial \mathbf{F}'}{\partial \eta} + \frac{\partial \mathbf{G}'}{\partial \zeta} = \frac{1}{Re}\left(\frac{\partial \mathbf{E}'_\mathbf{v}}{\partial \xi} + \frac{\partial \mathbf{F}'_\mathbf{v}}{\partial \eta} + \frac{\partial \mathbf{G}'_\mathbf{v}}{\partial \zeta}\right) \tag{1}$$

where Re is the Reynolds number and

$$\mathbf{Q}' = \frac{\mathbf{Q}}{J} \tag{2}$$

$$\mathbf{E}' = \frac{1}{J}(\xi_t \mathbf{Q} + \xi_x \mathbf{E} + \xi_y \mathbf{F} + \xi_z \mathbf{G}) \tag{3}$$

$$\mathbf{F}' = \frac{1}{J}(\eta_t \mathbf{Q} + \eta_x \mathbf{E} + \eta_y \mathbf{F} + \eta_z \mathbf{G}) \tag{4}$$

$$\mathbf{G}' = \frac{1}{J}(\zeta_t \mathbf{Q} + \zeta_x \mathbf{E} + \zeta_y \mathbf{F} + \zeta_z \mathbf{G}) \tag{5}$$

$$\mathbf{E}'_\mathbf{v} = \frac{1}{J}(\xi_x \mathbf{E}_\mathbf{v} + \xi_y \mathbf{F}_\mathbf{v} + \xi_z \mathbf{G}_\mathbf{v}) \tag{6}$$

$$\mathbf{F}'_\mathbf{v} = \frac{1}{J}(\eta_x \mathbf{E}_\mathbf{v} + \eta_y \mathbf{F}_\mathbf{v} + \eta_z \mathbf{G}_\mathbf{v}) \tag{7}$$

$$\mathbf{G}'_\mathbf{v} = \frac{1}{J}(\zeta_x \mathbf{E}_\mathbf{v} + \zeta_y \mathbf{F}_\mathbf{v} + \zeta_z \mathbf{G}_\mathbf{v}) \tag{8}$$

where J is the transformation Jacobian. The variable vector $\mathbf{Q}$, and inviscid flux vectors $\mathbf{E}$, $\mathbf{F}$, and $\mathbf{G}$ are written as

$$\mathbf{Q} = \begin{bmatrix} \bar{\rho} \\ \bar{\rho}\tilde{u} \\ \bar{\rho}\tilde{v} \\ \bar{\rho}\tilde{w} \\ \bar{\rho}\tilde{e} \end{bmatrix}, \mathbf{E} = \begin{bmatrix} \bar{\rho}\tilde{u} \\ \bar{\rho}\tilde{u}\tilde{u} + \bar{p} \\ \bar{\rho}\tilde{u}\tilde{v} \\ \bar{\rho}\tilde{u}\tilde{w} \\ (\bar{\rho}\tilde{e} + \bar{p})\tilde{u} \end{bmatrix}, \mathbf{F} = \begin{bmatrix} \bar{\rho}\tilde{v} \\ \bar{\rho}\tilde{v}\tilde{u} \\ \bar{\rho}\tilde{v}\tilde{v} + \bar{p} \\ \bar{\rho}\tilde{v}\tilde{w} \\ (\bar{\rho}\tilde{e} + \bar{p})\tilde{v} \end{bmatrix}, \mathbf{G} = \begin{bmatrix} \bar{\rho}w \\ \bar{\rho}\tilde{w}\tilde{u} \\ \bar{\rho}\tilde{w}\tilde{v} \\ \bar{\rho}\tilde{w}\tilde{w} + \bar{p} \\ (\bar{\rho}\tilde{e} + \bar{p})\tilde{w} \end{bmatrix},$$

where ρ is the density, u, v, and w are the Cartesian velocity components in x, y and z directions, p is the static pressure, and e is the total energy per unit mass. The overbar denotes the spatial filtered quantity, tilde denotes the Favre-filtered quantity. All the flow variable in above equations are non-dimensionlized by using the freestream quantities and a reference length L. $\mathbf{E}'$, $\mathbf{F}'$, and $\mathbf{G}'$ are the inviscid fluxes at the moving grid system and can be expressed as

$$\mathbf{E}' = \begin{bmatrix} \bar\rho U \\ \bar\rho\tilde{u}U + l_x\bar{p} \\ \bar\rho\tilde{v}U + l_y\bar{p} \\ \bar\rho\tilde{w}U + l_z\bar{p} \\ (\bar\rho\tilde{e} + \bar{p})U - l_t\bar{p} \end{bmatrix}, \mathbf{F}' = \begin{bmatrix} \bar\rho V \\ \bar\rho\tilde{u}V + m_x\bar{p} \\ \bar\rho\tilde{v}V + m_y\bar{p} \\ \bar\rho\tilde{w}V + m_z\bar{p} \\ (\bar\rho\tilde{e} + \bar{p})V - m_t\bar{p} \end{bmatrix}, \mathbf{G}' = \begin{bmatrix} \bar\rho W \\ \bar\rho\tilde{u}W + n_x\bar{p} \\ \bar\rho\tilde{v}W + n_y\bar{p} \\ \bar\rho\tilde{w}W + n_z\bar{p} \\ (\bar\rho\tilde{e} + \bar{p})W - n_t\bar{p} \end{bmatrix},$$

where U, V and W are the contravariant velocities in ξ, η and ζ directions, and defined as

$$\begin{aligned} U &= l_t + \mathbf{l} \bullet \mathbf{V} = l_t + l_x\tilde{u} + l_y\tilde{v} + l_z\tilde{w} \\ V &= m_t + \mathbf{m} \bullet \mathbf{V} = m_t + m_x\tilde{u} + m_y\tilde{v} + m_z\tilde{w} \\ W &= n_t + \mathbf{n} \bullet \mathbf{V} = n_t + n_x\tilde{u} + n_y\tilde{v} + n_z\tilde{w} \end{aligned} \tag{9}$$

where l_t, m_t and n_t are the components of the interface contravariant velocity of the control volume in ξ, η and ζ directions respectively, $\mathbf{l}$, $\mathbf{m}$ and $\mathbf{n}$ are the normal vectors located at the centers of ξ, η and ζ interfaces of the control volume with their magnitudes equal to the surface areas and pointing to the directions of increasing ξ, η and ζ. These quantities are defined as

$$l_t = \frac{\xi_t}{J}, \quad m_t = \frac{\eta_t}{J}, \quad n_t = \frac{\zeta_t}{J} \tag{10}$$

$$\mathbf{l} = \frac{\nabla\xi}{J}, \quad \mathbf{m} = \frac{\nabla\eta}{J}, \quad \mathbf{n} = \frac{\nabla\zeta}{J} \tag{11}$$

and the viscous flux vectors are given by

$$\mathbf{E_v} = \begin{bmatrix} 0 \\ \bar\tau_{xx} + \sigma_{xx} \\ \bar\tau_{xy} + \sigma_{xy} \\ \bar\tau_{xz} + \sigma_{xz} \\ Q_x \end{bmatrix}, \mathbf{F_v} = \begin{bmatrix} 0 \\ \bar\tau_{yx} + \sigma_{yx} \\ \bar\tau_{yy} + \sigma_{yy} \\ \bar\tau_{yz} + \sigma_{yz} \\ Q_y \end{bmatrix}, \mathbf{G_v} = \begin{bmatrix} 0 \\ \bar\tau_{zx} + \sigma_{zx} \\ \bar\tau_{zy} + \sigma_{zy} \\ \bar\tau_{zz} + \sigma_{zz} \\ Q_z \end{bmatrix}$$

Let subscript 1, 2 and 3 represent the coordinates, x, y, and z, and use Einstein summation convention, the shear-stress, the subgrid scale stress tensor, and Q_x, Q_y, Q_z terms in non-dimensional forms can be expressed in tensor form as

$$\bar\tau_{ij} = \frac{2}{3}\tilde\mu\frac{\partial\tilde{u}_k}{\partial x_k}\delta_{ij} + \tilde\mu(\frac{\partial\tilde{u}_i}{\partial x_j} + \frac{\partial\tilde{u}_j}{\partial x_i}) \tag{12}$$

$$\sigma_{ij} = -\bar{\rho}(\widetilde{u_i u_j} - \tilde{u}_i \tilde{u}_j) \tag{13}$$

$$Q_i = \tilde{u}_j(\bar{\tau}_{ij} + \sigma_{ij}) - \bar{q}_i + \Phi_i \tag{14}$$

In Eq.(12), the viscosity μ is the molecular viscosity and is determined by Sutherland law. Φ_i and $\bar{q}_i$ are the subscale heat flux and the mean molecular heat flux respectively, and take the forms:

$$\Phi_i = -C_p \bar{\rho}(\widetilde{u_i T} - \tilde{u}_i \tilde{T}) \tag{15}$$

$$\bar{q}_i = -\frac{C_p \tilde{\mu}}{Pr} \frac{\partial \tilde{T}}{\partial x_i} \tag{16}$$

where T is the temperature, C_p is the specific heat measured under constant pressure, and Pr is the Prandtl number. The equation of state closes the system as follow,

$$\bar{\rho}\tilde{e} = \frac{\tilde{p}}{(\gamma - 1)} + \frac{1}{2}\bar{\rho}(\tilde{u}^2 + \tilde{v}^2 + \tilde{w}^2) + \bar{\rho}k \tag{17}$$

where γ is the ratio of specific heats, $\bar{\rho}k$ is the subscale turbulence kinetic energy per unit volume and takes the form:

$$\bar{\rho}k = \frac{1}{2}\bar{\rho}(\widetilde{u_i u_i} - \tilde{u}_i \tilde{u}_i) \tag{18}$$

In the present study, the term $\bar{\rho}k$ is neglected based on the assumption that its effect is small.

2.2 Detached Eddy Simulation

The DES suggested by Spalart et al.[23] is based on the Spalart-Allmaras one-equation turbulence model [10], which can be expressed in generalized coordinates as

$$\frac{\partial \frac{1}{J}\rho\tilde{\nu}}{\partial t} + \frac{\partial \rho\tilde{\nu}U}{\partial \xi} + \frac{\partial \rho\tilde{\nu}V}{\partial \eta} + \frac{\partial \rho\tilde{\nu}W}{\partial \zeta} = \frac{1}{Re}\left[\frac{\partial \frac{\rho}{\sigma}(\nu + \tilde{\nu})\mathbf{l} \bullet \nabla\tilde{\nu}}{\partial \xi} + \right.$$

$$\left. \frac{\partial \frac{\rho}{\sigma}(\nu + \tilde{\nu})\mathbf{m} \bullet \nabla\tilde{\nu}}{\partial \eta} + \frac{\partial \frac{\rho}{\sigma}(\nu + \tilde{\nu})\mathbf{n} \bullet \nabla\tilde{\nu}}{\partial \zeta} + \frac{1}{J}S_\nu \right] \tag{19}$$

where

$$S_\nu = \rho C_{b1}(1 - f_{t2})\tilde{S}\tilde{\nu} + \frac{1}{Re}\left[-\rho\left(C_{w1}f_w - \frac{C_{b1}}{\kappa^2}f_{t2}\right)\left(\frac{\tilde{\nu}}{d}\right)^2 + \right.$$

$$\left.\frac{\rho}{\sigma}C_{b2}(\nabla\tilde{\nu})^2 - \frac{1}{\sigma}(\nu + \tilde{\nu})\nabla\tilde{\nu} \bullet \nabla\rho\right] + Re\left[\rho f_{t1}(\triangle)^2\right] \tag{20}$$

The turbulent eddy viscosity is calculated from

$$\nu_t = \tilde{\nu} f_{v1}, \quad f_{v1} = \frac{\chi^3}{\chi^3 + c_{v1}^3}, \quad \chi = \frac{\tilde{\nu}}{\nu} \tag{21}$$

where ν is the molecular viscosity. The production term is expressed as

$$\tilde{S} = S + \frac{\tilde{\nu}}{k^2 d^2} f_{v2}, \qquad f_{v2} = 1 - \frac{\chi}{1 + \chi f_{v1}}$$

where S is the magnitude of the vorticity. The DES is formulated by replacing the distance to the nearest wall, d, in the Spalart-Allmaras model with a modified distance

$$\tilde{d} = min(d, C_{DES}\Delta) \tag{22}$$

where Δ is the largest spacing of the grid cell and C_{DES} is a constant. This mechanism enables DES to behave as a RANS model in the near-wall regions, and the LES away from the wall. Consequently, the subgrid scale stress tensor can be modeled in the following way:

$$\sigma_{ij} = \mu_{DES}\left(\frac{\partial\tilde{u}_i}{\partial x_j} + \frac{\partial\tilde{u}_j}{\partial x_i} - \frac{2}{3}\frac{\partial\tilde{u}_k}{\partial x_k}\delta_{ij}\right) \tag{23}$$

where

$$\mu_{DES} = \bar{\rho}\nu_t = \bar{\rho}\tilde{\nu} f_{v1} \tag{24}$$

The subscale heat flux can calculated using the following equation:

$$\Phi_i = \frac{C_p \mu_{DES}}{Pr_t}\frac{\partial\tilde{T}}{\partial x_i} \tag{25}$$

where Pr_t is the turbulent Prandtl number. More details of the Spalart DES model can be found in[23, 28, 24].

2.3 Delayed-Detached-Eddy Simulation[21]

To overcome the modeled-stress depletion (MSD) problem and make the DES limiter independent of grid spacing, the DDES model is formed by modifying the length scale in the SA turbulence model. This is achieved by re-defining the distance to the nearest wall, $\tilde{d}$ as

$$\tilde{d} = d - f_d max(0, d - C_{DES}\Delta) \tag{26}$$

where f_d is a coefficient that can be estimated by the following equations[21]:

$$f_d = 1 - tanh((8r_d)^3), \qquad r_d = \frac{\tilde{\nu} + \nu}{\sqrt{U_{i,j}U_{i,j}}\kappa^2 d^2} \tag{27}$$

where $U_{i,j}$ is the velocity gradients, κ is the Karman constant, and d is the distance to the nearest wall.

2.4 Roe's Riemann Solver on Moving Grid System

An accurate Riemann solver is necessary to resolve the shock wave and wall boundary layer in the flow field. The Roe scheme[29] is used to evaluate the inviscid fluxes with the 5rd order WENO scheme[25, 26]. In the present study, the original Roe scheme is extended to moving grid system as the following, for example, in ξ direction:

$$\mathbf{E}'_{i+\frac{1}{2}} = \frac{1}{2}[\mathbf{E}''(\mathbf{Q_L}) + \mathbf{E}''(\mathbf{Q_R}) + \mathbf{Q_L}\xi_{tL} + \mathbf{Q_R}\xi_{tR} - |\tilde{\mathbf{A}}|(\mathbf{Q_R} - \mathbf{Q_L})]_{i+\frac{1}{2}} \tag{28}$$

where $\mathbf{Q_L}$ and $\mathbf{Q_R}$ are the reconstructed variables to the left and right sides of the cell face, ξ_{tL} and ξ_{tR} are the reconstructed grid velocity component in ξ direction to the left and right sides of the cell interface $i + \frac{1}{2}$, $\mathbf{A}$ is the Jacobian matrix, $\mathbf{A} = \frac{\partial \mathbf{E}'}{\partial \mathbf{Q}}$ and it takes the form as $\mathbf{A} = \mathbf{T}\boldsymbol{\Lambda}\mathbf{T}^{-1}$, $\mathbf{T}$ is the right eigenvector matrix of $\mathbf{A}$, $\boldsymbol{\Lambda}$ is the eigenvalue matrix of $\mathbf{A}$, and

$$\tilde{\mathbf{A}} = \tilde{\mathbf{T}}\tilde{\boldsymbol{\Lambda}}\tilde{\mathbf{T}}^{-1} \tag{29}$$

where $\tilde{\boldsymbol{\Lambda}}$ is the eigenvalue matrix on moving grid system with the eigenvalues of

$$(\tilde{U} + \tilde{C}, \tilde{U} - \tilde{C}, \tilde{U}, \tilde{U}, \tilde{U}) \tag{30}$$

where $\tilde{U}$ is the contravariant velocity in ξ direction on moving grid,

$$\tilde{U} = \tilde{\xi}_t + \xi_x \tilde{u} + \xi_y \tilde{v} + \xi_z \tilde{w} \tag{31}$$

$\tilde{C}$ is the speed of sound corresponding to the contravariant velocity:

$$\tilde{C} = \tilde{c}\sqrt{\xi_x^2 + \xi_y^2 + \xi_z^2} \tag{32}$$

where $c = \sqrt{\gamma RT}$ is the physical speed of sound. The $\sim$ stands for the Roe-averaged quantities. For example,

$$\tilde{\xi}_t = (\xi_{tL} + \xi_{tR}\sqrt{\rho_R/\rho_L})/(1 + \sqrt{\rho_R/\rho_L}) \tag{33}$$

The grid velocity is evaluated at the center of each cell and is determined by the averaged value that counts the movement of the eight vertexes. The grid velocity is also reconstructed with a 5th order finite difference WENO scheme.

2.5 Time Marching Scheme

The unsteady compressible Navier-Stokes equations (1) coupled to the Spalart-Allmaras turbulence equation (19) are solved using the finite difference method with the concept of dual time stepping suggested by Jameson[2]. A pseudo temporal term $\frac{\partial \mathbf{Q}}{\partial \tau}$ is added to the governing equation (1). This term vanishes at the end of each physical time step, and has no influence on the accuracy of the solution. However, instead of using the explicit scheme as in [2], an implicit pseudo time marching scheme using line Gauss-Seidel iteration is employed to achieve high convergence rate. For unsteady time accurate computations, the temporal term is discretized implicitly using a three point, backward differencing as the following

$$\frac{\partial \mathbf{Q}}{\partial t} = \frac{3Q^{n+1} - 4Q^n + Q^{n-1}}{2\Delta t} \tag{34}$$

Where n is the time level index. The pseudo temporal term is discretized with first order Euler scheme. Let m stand for the iteration index within a physical time step, the semi-discretized governing equation (1) can be expressed as

$$[(\frac{1}{\Delta\tau} + \frac{1.5}{\Delta t})I - (\frac{\partial R}{\partial Q})^{n+1,m}]\delta Q^{n+1,m+1} = R^{n+1,m} - \frac{3Q^{n+1,m} - 4Q^n + Q^{n-1}}{2\Delta t} \tag{35}$$

where the $\Delta\tau$ is the pseudo time step, R is the net flux evaluated at a grid point. Equation (35) is solved using the unfactored line Gauss-Seidel iteration.

2.6 Boundary Conditions

The boundary conditions used in the simulation are as follows:

(1) Upstream boundary conditions: The outer boundary (see Fig.4) is divided into upstream and downstream boundaries according to whether the direction of its segment is toward or backward to the incoming flow direction. At the upstream boundary, it is assumed that the streamwise velocity u is uniform, transverse velocity $v = 0$, and spanwise velocity $w = 0$. Other primitive variables are specified according to the freestream condition except the pressure which is extrapolated from the interior.

(2) Downstream boundary conditions: All the flow quantities are extrapolated from the interior except the pressure which is set to be its freestream value.

(3) Solid wall boundary conditions: At moving boundary surface, the no-slip condition is enforced by extrapolating the velocity between the phantom and interior cells,

$$u_0 = 2\dot{x}_b - u_1, \qquad v_0 = 2\dot{y}_b - v_1, \qquad w_0 = 2\dot{z}_b - w_1 \tag{36}$$

where u_0, v_0 and w_0 denote the velocity at phantom cells, u_1, v_1 and w_1 denote the velocity at the $1st$ interior cells close to the boundary, and u_b, v_b and w_b are the velocity components of the moving boundary.

If the wall surface is in η direction, the other two conditions to be imposed on the solid wall are the adiabatic wall condition and the inviscid normal momentum equation[30] as follows,

$$\frac{\partial T}{\partial \eta} = 0, \qquad \frac{\partial p}{\partial \eta} = -\left(\frac{\rho}{\eta_x^2 + \eta_y^2 + \eta_z^2}\right)(\eta_x \ddot{x}_b + \eta_y \ddot{y}_b + \eta_z \ddot{z}_b) \tag{37}$$

3 Modal Approach of Three Dimensional Wing

The calculation based on fully coupled iteration is CPU expensive, especially for three dimensional applications. The modal approach can save CPU time significantly by solving modal displacement equations, Eq. (41), instead of the original structural equations, Eq. (38), which is usually solved by using finite element method. In the modal approach, the structural mode shapes can be predetermined by using a separate finite element structural solver. Once the several mode shapes of interest are obtained, the physical displacements can be calculated just by solving those simplified linear equations, Eq. (41) and Eq. (40). In present study, the first five mode shapes provided in

Ref.[31] are used to model the wing structure. These pre-calculated mode shapes are obtained on a structural grid system and are transformed to the CFD grid system by using a 3rd order polynomial fitting procedure. The procedure is only performed once and then the mode shapes for CFD grid system are stored in the code throughout the simulation. To validate the structural model used in the present study, the dynamic responses of a flexible plate wing is calculated and compared with the results by using the finite element solver ANSYS. The plate wing has the same outline as the AGARD wing 445.6, and its first mode natural vibration frequency is nearly the same as the corresponding one of the AGARD wing 445.6. The numerical predictions by the present structural solver with first five mode shapes agree excellently with the results obtained by ANSYS using first five mode shapes and the full structural model [20].

The governing equation of the solid structure motion can be written as,

$$\mathbf{M}\frac{d^2\mathbf{u}}{dt^2} + \mathbf{C}\frac{d\mathbf{u}}{dt} + \mathbf{K}\mathbf{u} = \mathbf{f} \tag{38}$$

where $\mathbf{M}$, $\mathbf{C}$ and $\mathbf{K}$ are the mass, damping, and stiffness matrices of the solid respectively, $\mathbf{u}$ is the displacement vector and $\mathbf{f}$ is the force exerted on the surface node points of the solid. In a modal approach, the modal decomposition of the structure motion can be expressed as follows:

$$\mathbf{K}\phi_j = \lambda_j \mathbf{M}\phi_j \tag{39}$$

where $\mathbf{\Lambda}$ is eigenvalue matrix, $\mathbf{\Lambda} = diag[\lambda_1, \cdots, \lambda_j, \cdots, \lambda_{3N}]$, and jth eigenvalue $\lambda_j = {\omega_j}^2$, ω_j is the natural frequency of jth mode, and the mode shape matrix $\mathbf{\Phi} = [\phi_1, \cdots, \phi_j, \cdots, \phi_{3N}]$, N is the total number of node points of the structural model.

Equation (39) can be solved by using a finite element solver (e.g. ANSYS) to obtain its finite number of mode shapes ϕ_j. The first five mode shapes will be used in this paper to calculate the displacement of the structure such that,

$$\mathbf{u}(t) = \sum_j a_j(t)\phi_j = \mathbf{\Phi}\mathbf{a} \tag{40}$$

where $\mathbf{a} = [a_1, a_2, a_3, a_4, a_5]^T$. The normalized modal equations of structure motion may be expressed as

$$\frac{d^2 a_j}{dt^{*2}} + 2\zeta_j\left(\frac{\omega_j}{\omega_\alpha}\right)\frac{da_j}{dt^*} + \left(\frac{\omega_j}{\omega_\alpha}\right)^2 a_j = \phi_j^{*T}\mathbf{f}^* V^* \left(\frac{b_s}{L}\right)^2 \frac{\bar{m}}{v^*} \tag{41}$$

where the dimensionless quantities are denoted by an asterisk, ζ_j is modal damping ratio, ω_α is the natural frequency in pitch, b_s is the streamwise semichord measured at wing root, L is the reference length, $\bar{m}$ is the measured wing panel mass, v is the volume of a conical frustum having streamwise root chord as lower base diameter, streamwise tip chord as upper base diameter, and panel span as height, $V^* = \frac{U_\infty}{b_s \omega_\alpha \sqrt{\bar{\mu}}}$, U_∞ is the freestream velocity, and $\bar{\mu}$ is the mass ratio defined as $\frac{\bar{m}}{\rho v}$. Then the equations are transformed to a state form and expressed as:

$$[\mathbf{M}]\frac{\partial \{\mathbf{S}\}}{\partial t} + [\mathbf{K}]\{\mathbf{S}\} = \mathbf{q} \tag{42}$$

where

$$\mathbf{S} = \begin{pmatrix} a_j \\ \dot{a}_j \end{pmatrix}, \ \mathbf{M} = [I], \ \mathbf{K} = \begin{pmatrix} 0 & -1 \\ \left(\frac{\omega_j}{\omega_\alpha}\right)^2 & 2\zeta\left(\frac{\omega_j}{\omega_\alpha}\right) \end{pmatrix}, \ \mathbf{q} = \begin{pmatrix} 0 \\ \phi_j^{*T}\mathbf{f}^* V^* \left(\frac{b_s}{L}\right)^2 \frac{\bar{m}}{v^*} \end{pmatrix}.$$

To couple the structural equations with the equations of flow motion and solve them implicitly in each physical time step, above equations are discretized and integrated in a manner consistent with Equation (35) to yield

$$\left(\frac{1}{\Delta\tau}\mathbf{I} + \frac{1.5}{\Delta t}\mathbf{M} + \mathbf{K}\right)\delta S^{n+1,m+1} = -\mathbf{M}\frac{3\mathbf{S}^{n+1,m} - 4\mathbf{S}^{n} + \mathbf{S}^{n-1}}{2\Delta t} - \mathbf{K}\mathbf{S}^{n+1,m} + \mathbf{q}^{n+1,m+1} \tag{43}$$

where n is the physical time level index while m stands for the pseudo time index. The detailed derivation of the modal equations can be found in Ref.[20], and the coupling procedure between the fluid and structural systems is given in the following section.

4 Fully Coupled FSI Procedure

In the fully-coupled computation, the remeshing is performed in each iteration. Therefore, a CPU time efficient algebraic grid deformation method is employed in the computation instead of the commonly-used grid generation method in which the Poisson equation is solved for grid points. It is shown that the method can maintain the initial grid quality and keep almost the same mesh distribution around the wing surface. The details on the implementation can be found in Ref.[20].

In order to reduce or avoid the error caused by the mixed temporal and spatial derivatives after a discretization procedure, the geometric conservation law suggested by Thomas et al.[32] needs to be enforced. To implement this option in the flow solver, the following term should be added to the right-hand side of Eq.(1):

$$\mathbf{S} = \mathbf{Q}\left[\frac{\partial J^{-1}}{\partial t} + \left(\frac{\xi_t}{J}\right)_\xi + \left(\frac{\eta_t}{J}\right)_\eta + \left(\frac{\zeta_t}{J}\right)_\zeta\right] \tag{44}$$

To rigorously simulate fluid-structural interactions, the equations of flow motion and structural response need to be solved simultaneously within each iteration in a fully coupled manner. The procedure of the fully coupled fluid-structure interaction can be seen in the flow chart given in Figure 1.

The code is developed as a multiblock flow solver for massively paralle computers. A general sub-domain bounadry mapping procedure is applied [33]. Both fluid and structural information at the hallo cells is exachanged asynchronously after each iteration. In other words, the send and receive calls return immediately when the message is still processed. The communication between blocks is operated by MPI.

5 Results and Discussion

The result of steady state transonic ONERA M6 wing is calculated first in order to validate the DDES CFD solver. Then, the DDES is performed for prediction of the flutter boundary of the AGARD wing 445.6 in a transonic flow.

5.1 Steady State Transonic ONERA M6 wing

As a validation of the three dimensional DDES solver for a transonic wing, the steady state solution of the transonic ONERA M6 wing is calculated. The freestream conditions for this study are listed in Table 1 below.

Table 1: Free-stream condition for ONERA M6 wing

Mach number	0.8395
Static Pressure (psia)	12.2913
Temperature (R)	447.0
Angle-of-Attack (deg)	0.0
Reynolds Number	19.7×10^{6}

This case is calculated using an O-type grid with the dimension of 144 (around wing) ×60 (normal to the wing) ×40 (spanwise). The far field boundary is located 15 chords away from the chord center of the wing. The surface mesh of the wing is depicted in Figure 2.

The computed surface pressure distributions at various cross sections are shown in Figure 3, together with the experimental data given by Schmitt et al. [34]. The location of $z/b = 0.2$ is near the root, and $z/b = 0.99$ is at wing tip. Overall, very good agreement is obtained between the computation and experiment for each cross-section.

5.2 AGARD Wing 445.6 Flutter

The DDES is conducted for predicting AGARD Wing 445.6 flutter boundary at $M_\infty = 0.96$. This wing has a quarter-chord sweep angle of 45 degree, an aspect ratio of 1.65, a taper ratio of 0.6576, and a NACA65A004 airfoil section in the streamwise direction. The weakened wing model (Model 3) listed in [31] is chosen for this study. The geometry of the wing and its first six mode shapes as well as the experimental flutter results are also provided in the same report [31]. The wing structure is modeled by its first five natural vibration modes in the present computation. A multiblock grid system for the AGARD wing simulations is generated and shown in Fig.4. The grid system consists of 8 blocks with 9×61×41 grid points/block in ξ, η, ζ direction respectively, and another 8 blocks with 10×61×41 grid points/block.

The simulation starts with the stationary rigid body wing model. After the steady state flow field around the wing is fully developed, the rigid body wing is switched to the flexible wing model. As a small imposed perturbation, the first mode displacement of the structural motion is set into sinusoidal motion for approximately one cycle with the maximum amplitude of 0.001 and the first mode frequency of the wing. Then the wing is allowed to deflect in response to the dynamic force load. Within each physical time step, the solution is usually converged with 15-30 iterations.

In Figures 5 through 7 the time histories of generalized displacements of the AGARD wing 445.6 at $M_\infty = 0.96$ are plotted for three different V^*. In these figures, from $V^* = 0.264$ to $V^* = 0.303$, the plots correspond to the damped, neutral, and diverging responses respectively. When the value of V^* is smaller than the critical value on the flutter boundary, the amplitudes of all modes decrease in time corresponding to the damped response as shown in Figure 5. Once the value of V^* coincides with or is close to the critical value, the neutral response appears as shown in Fig. 6. When the value of V^* is above the neutral stability point, the amplitudes of first five modes grow very fast, a diverging response is reached as shown in Fig. 7. Fig.8 shows the time histories of the wing tip plunging and pitching displacements at $M_\infty = 0.96$ and $V^* = 0.303$. The plunging displacement is measured at the center of the wing tip cross-section, its neutral position is equal to zore. The pitching displacement (angle of attach) is calculated by using the leading and trailing positions of the wing tip cross-section. The plunging and pitching displacements oscillate in opposite phase. The deformed wing surfaces when the wing tip is located at the uppermost and lowermost positions for $V^* = 0.303$ are depicted in Fig.9. For the same moment, the lower and upper wing surface profile contours are shown in Fig.10, and the pressure contours on the lower and upper wing surfaces are shown in Fig.11.

For a given Mach number, several runs with different V^* are needed to determine the location of the flutter boundary using a bisection method. To obtain different value of V^*, the total pressure at the inlet changes accordingly while the total temperature is fixed. At $M_\infty = 0.96$, the location of the predicated flutter boundary is about 0.285 which is consistent with the experimental value of 0.3076 provided by Ref.[31] and the computed value of 0.263 found in Ref.[14].

6 Conclusion

Delayed-detached-eddy simulation of 3-D fluid-structural interaction is presented for predicting the AGARD Wing 445.6 flutter boundary in a transonic flow. A dual-time step implicit unfactored Gauss-Seidel iteration with Roe scheme are employed for the flow solver. A modal approach is used for solving structural response. The flow and structural solvers are fully coupled vis successive iterations within each physical time step. The method is developed as a multiblock code in a MPI parallel environment. The computed flutter boundary of AGARD Wing 445.6 in a transonic flow is presented, and the flutter speed agrees well with the experimental data and computed result found in literature. The damped, neutral, and diverging aeroelastic responses, and transonic dip are well captured in a transonic flow. It indicates that the DDES can provide a more accurate turbulence closure in aeroelastic analysis.

7 Acknowledgment

This work is supported by GUIde IV consortium grant 09-1010.

References

[1] O. Bendiksen and K. Kousen, "Transonic Flutter Analysis Using the Euler Equations." AIAA Paper 87-0911, 1987.

[2] A. Jameson, "Time Dependent Calculations Using Multigrid with Application to Unsteady Flows past Airfoils and Wings." AIAA Paper 91-1596, 1991.

[3] J. Alonso, L. Martinelli, and A. Jameson, "Multigrid Unsteady Navier-Stokes Calculations with Aeroelastic Applications." AIAA Paper 95-0048, 1995.

[4] G. Srinivasan, J. Ekaterinaris, and W. McCroskey, "Evaluation of Turbulence Models for Unsteady Flows of an Oscillating Airfoil," *Journal of Computers and Fluids*, vol. 24, pp. 833–861, 1995.

[5] B. Baldwin and H. Lomax, “Thin-Layer Approximation and Algebraic Model for Separated Turbulent flows.” AIAA Paper 78-257, 1978.

[6] V. Yakhot and S. Orzag, “Renormalization group analysis of turbulence. I. Basic theory,” *Journal of Scientific Computing*, vol. 1, pp. 3–51, 1986.

[7] D. Johnson and L. King, “A mathematically simple turbulence closure model for attached and separated turbulent boundary layers,” *AIAA Journal*, vol. 23, p. 1684, 1985.

[8] D. Johnson, “Nonequilibrium algebraic turbulence modeling considerations for transonic airfoil and wings,” 1992.

[9] B. Baldwin and A. Barth, “A one-equation turbulence transport model for high reynolds number wall-bounded flows.” AIAA Paper 91-0610, 1991.

[10] P. Spalart and S. Allmaras, “A one-equation turbulence model for aerodynamic flows.” AIAA Paper 92-0439, 1992.

[11] B. B. Prananta, H. M. H. L., and Z. R. J., “Two-Dimensional Transonic Aeroelastic Analysis Using Thin-Layer Navier-Stokes Method,” *Journal of Fluid and Structures*, vol. 12, pp. 655–676, 1998.

[12] J. Bohbot, J. Garnier, S. Toumit, and D. Darracq, “Computation of the Flutter Boundary of an Airfoil with a Parallel Navier-Stokes Solver.” AIAA Paper 2001-0572, 2001.

[13] E. Lee-Rausch and J. Batina, “Calculation of AGARD Wing 445.6 Flutter Using Navier-Stokes Aerodynamics.” AIAA Paper 93-3476, 1993.

[14] F. Liu, Y. Zhu, H. Tsai, and A. Wong, “Calculation of Wing Flutter by a Coupled Fluid-Structure Method,” *Journal of Aircraft*, vol. 38, pp. 334–342, 2001.

[15] H. Doi and J. Alonso, “Fluid/Structure Coupled Aeroelastic Computations for Transonic Flows in Turbomachinery.” ASME Turbo Expo 2002, GT-2002-30313, 2002.

[16] J. Yao, A. Jameson, J. Alonso, and F. Liu, “Development and Validation of a Massively Parallel Flow Solver for Turbomachinery Flows.” AIAA Paper 00-0882, 2000.

[17] X.-Y. Chen, G.-C. Zha, and Z.-J. Hu, “Numerical Simulation of Flow Induced Vibration Based on Fully Coupled-Structural Interactions.” AIAA Paper 2004-2240, Juun 28 - July 1, 2004.

[18] X. Chen and G.-C. Zha, “Fully Coupled Fluid-Structural Interactions Using an Efficient High Solution Upwind Scheme,” *Journal of Fluid and Structure*, vol. 20, pp. 1105–1125, 2005.

[19] X.-Y. Chen, G.-C. Zha, and M.-T. Yang, “3D Simulation of a Transonic Wing Flutter using an Efficient High Resolution Upwind Scheme.” AIAA Paper 2006-3216, 2006.

[20] X.-Y. Chen, G.-C. Zha, and M.-T. Yang, “Numerical Simulation of 3-D Wing Flutter with Fully Coupled Fluid-Structural Interaction,” *Journal of Computers and Fluids*, vol. 35, pp. 856–867, 2007.

[21] P. Spalart, S. Deck, M. Shur, and K. Squires, “A New Version of Detached-Eddy Simulation, Resistant to Ambiguous Grid Densities,” *Theoritical and Computational Fluid Dynamics*, vol. 20, pp. 181–195, 2006.

[22] J. Deardorff, "A Numerical Study of Three-Dimensional Turbulent Channel Flow at Large Reynolds Numbers," *Journal of Fluid Mechanics*, vol. 41, pp. 453–480, 1970.

[23] P. Spalart, W. Jou, M. Streletes, and S. Allmaras, "Comments on the Feasibility of LES for Wings and a Hybrid RANS/LES Approach." First AFSOR International Conference on DNS/LES, 1997.

[24] B.-Y. Wang and G.-C. Zha, "Detached-Eddy Simulation of Transonic Airfoil Limited Cycle Oscillation with High Order WENO Scheme." AIAA Paper 2009-1507, 2008.

[25] Y.-Q. Shen, G.-C. Zha, and B.-Y. Wang, "Improvement of Stability and Accuracy of Implicit WENO Scheme," *AIAA Journal*, vol. 47, pp. 331–344, 2009.

[26] Y.-Q. Shen and G.-C. Zha, "Improvement of the WENO Scheme Smoothness Estimator," *International Journal for Numerical Methods in Fluids*, vol. DOI:10.1002/fld.2186, 2009.

[27] Y.-Q. Shen, G.-C. Zha, and X.-Y. Chen, "High Order Conservative Differencing for Viscous Terms and the Application to Vortex-Induced Vibration Flows," *Journal of Computational Physics*, vol. 228, pp. 8283–8300, 2009.

[28] B. Wang, G. Zha, and Y. Shen, "Detached-Eddy Simulations of a Circular Cylinder Using a Low Diffusion E-CUSP and High-Order WENO Scheme." AIAA Paper 2008-3855, 2008.

[29] P. Roe, "Approximate Riemann Solvers, Parameter Vectors, and Difference Schemes," *Journal of Computational Physics*, vol. 43, pp. 357–372, 1981.

[30] S. A. Morton, R. B. Melville, and M. R. Visbal, "Accuracy and Coupling Issues of Aeroelastic Navier-Stokes Solutions on Deforming Meshes." AIAA Paper-97-1085, 1997.

[31] E. Yates Jr., "Agard standard aeroelastic configurations for dynamic response i.-wing 445.6," Tech. Rep. AGARD Report No.765, AGARD, September 1985.

[32] P. Thomas and C. Lombard, "Geometric Conservation Law and Its Application to Flow Computations on Moving Grids," *AIAA Journal*, vol. 17, pp. 1030–1037, 1979.

[33] B.-Y. Wang, Z.-J. Hu, and G.-C. Zha, "A General Sub-Domain Boundary Mapping Procedure For Structured Grid CFD Parallel Computation," *AIAA Journal of Aerospace Computing, Information, and Communication*, vol. 5, pp. 425–447, 2008.

[34] V. Schmitt and F. Charpin, "Pressure Distributions on the onera-m6-wing at Transonic Mach Numbers," Tech. Rep. AGARD AR 138, AGARD, May 1979.

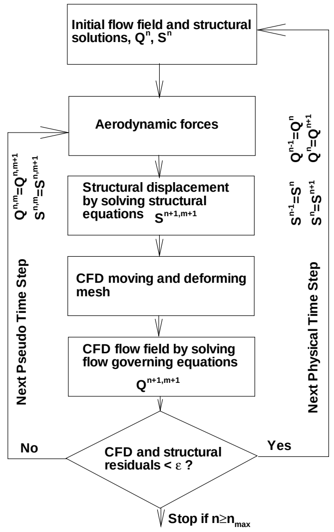

Figure 1: Fully coupled flow-structure interaction procedure

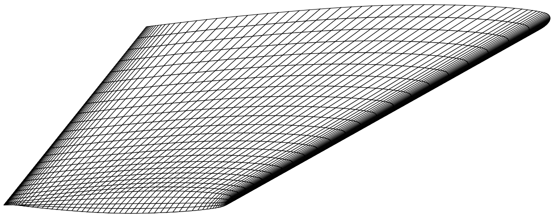

Figure 2: The mesh around the ONERA M6 wing surface.

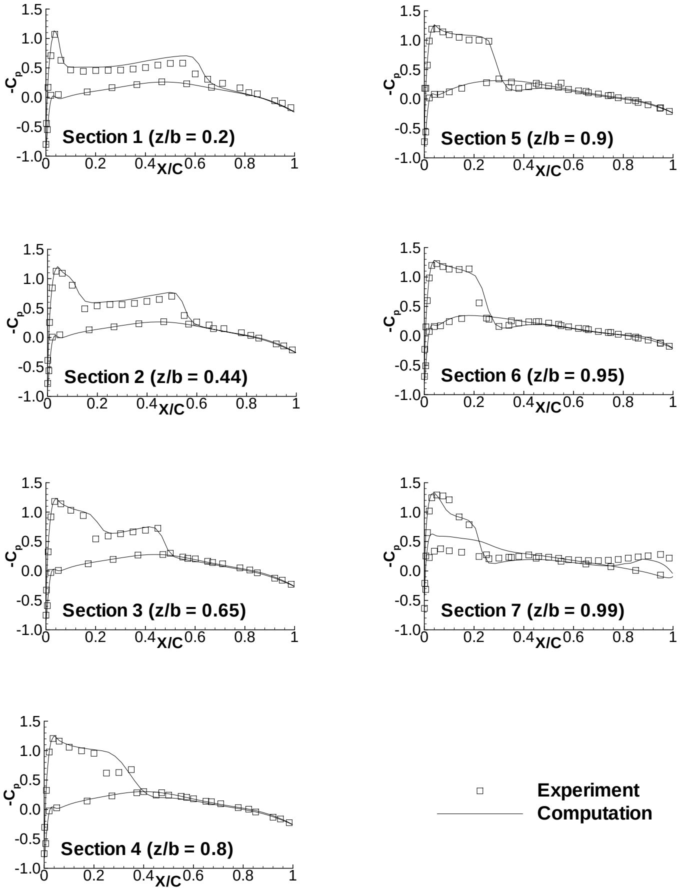

Figure 3: Pressure coefficients on the ONERA M6 wing surface at different cross-section.

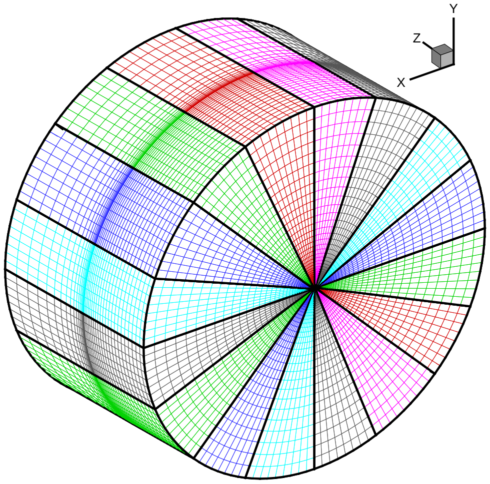

Figure 4: Multiblock grid system for the AGARD Wing 445.6.

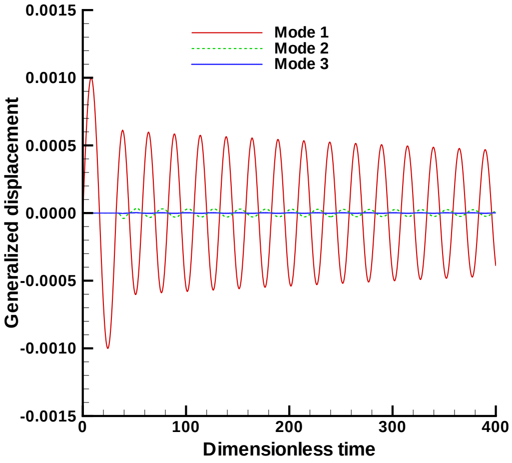

Figure 5: Time histories of the generalized displacements of first five modes for $M_\infty = 0.96$ and $V^* = 0.264$ - Damped response.

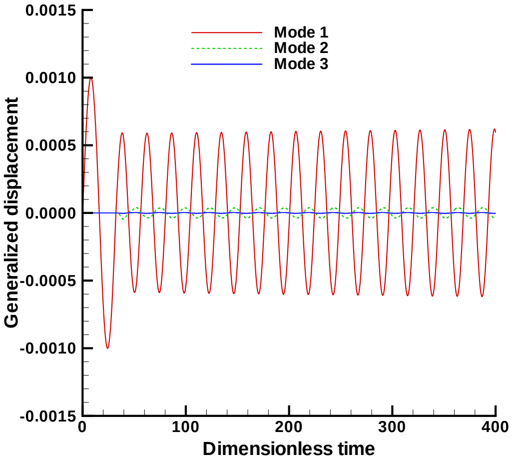

Figure 6: Time histories of the generalized displacements of first five modes for $M_\infty = 0.96$ and $V^* = 0.285$ - Neutrally stable response.

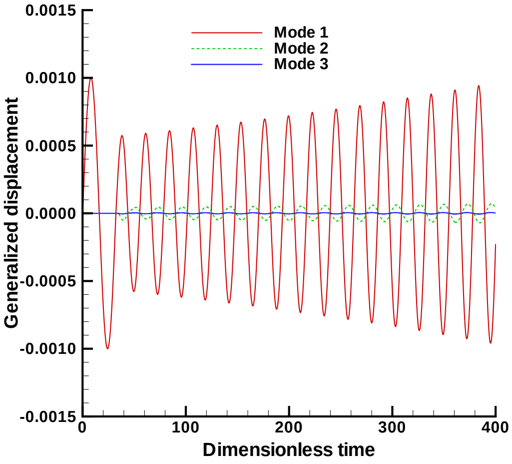

Figure 7: Time histories of the generalized displacements of first five modes for $M_\infty = 0.96$ and $V^* = 0.303$ - Diverging response.

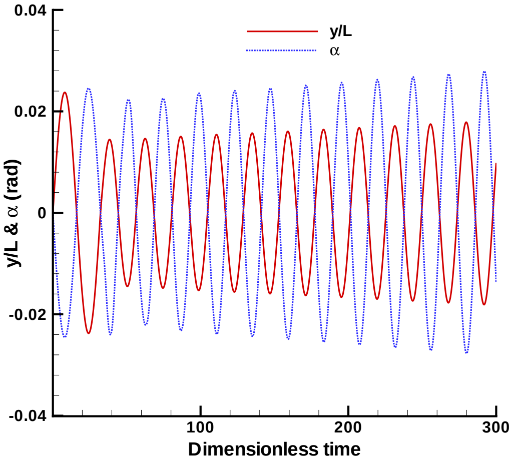

Figure 8: Time histories of the wing tip plunging and pitching displacements for $M_\infty = 0.96$ and $V^* = 0.303$.

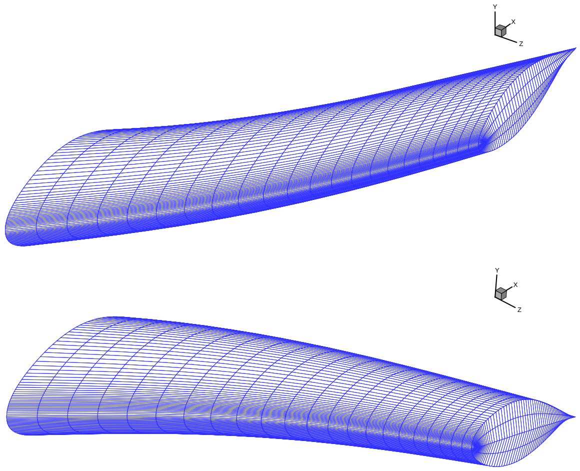

Figure 9: The deformed wing surfaces when the tip is located at the uppermost and lowermost positions for $M_\infty = 0.96$ and $V^* = 0.303$.

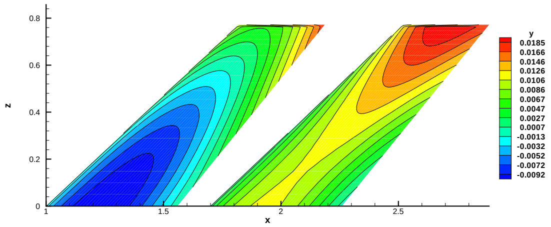

Figure 10: The lower (left) and upper (right) wing surface elevation contours when the tip is located at the uppermost position for $M_\infty = 0.96$ and $V^* = 0.303$.

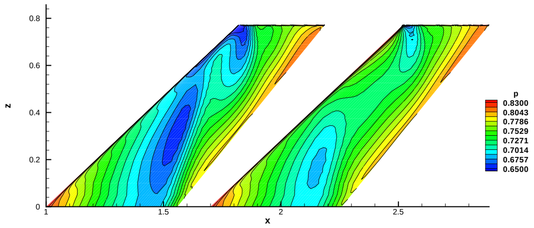

Figure 11: The pressure contours on lower (left) and upper (right) wing surfaces when the tip is located at the uppermost position for $M_\infty = 0.96$ and $V^* = 0.303$.